Seismic ocean thermometry of the Kuroshio Extension region

Shirui Peng[a], Jörn Callies[a], Wenbo Wu[a,b], and Zhongwen Zhan[a]

[a]California Institute of Technology, Pasadena, CA
[b]Woods Hole Oceanographic Institution, Woods Hole, MA

Key points

- Seismic *T* waves generated off Japan and received at Wake Island sample the Kuroshio Extension region
- Travel time changes between repeating earthquakes along the Japan Trench constrain the azimuth-dependent temperature change between events
- The data constrain deep temperature changes due to the meandering current, mesoscale eddies, and water mass rearrangements back to the 1990s

Corresponding author: Shirui Peng, speng2@caltech.edu

Abstract

Seismic ocean thermometry uses sound waves generated by repeating earthquakes to measure temperature change in the deep ocean. In this study, waves generated by earthquakes along the Japan Trench and received at Wake Island are used to constrain temperature variations in the Kuroshio Extension region. This region is characterized by energetic mesoscale eddies and large decadal variability, posing a challenging sampling problem for conventional ocean observations. The seismic measurements are obtained from a hydrophone station off and a seismic station on Wake Island, with the seismic station's digital record reaching back to 1997. These measurements are combined in an inversion for the time and azimuth dependence of the range-averaged deep temperatures, revealing lateral and temporal variations due to Kuroshio Extension meanders, mesoscale eddies, and decadal water mass rearrangements. These results highlight the potential of seismic ocean thermometry for better constraining the variability and trends in deep-ocean temperatures. By overcoming the aliasing problem of point measurements, these measurements complement existing ship- and float-based hydrographic measurements.

Plain language summary

The transfer of excess heat from the surface to the deep ocean is crucial in determining how rapidly global warming progresses. Despite progress, tracking the warming of the deep ocean remains an observational challenge because natural temperature variations can obscure the warming signal. These variations are especially intense on the western margin of ocean basins, where strong currents bring warm subtropical water poleward. These currents meander, shed eddies, and can switch between states every few years, all processes that lead to large local warming or cooling. This study helps alleviate the challenge to distinguish between these natural fluctuations and the forced signal by measuring deep ocean temperature using sound waves generated by earthquakes. We measure the travel time of these waves between Japan and Wake Island in historical seismic and acoustic records going back to the late 1990s, sampling one such current system. Because the waves travel faster in warmer water, they arrive slightly earlier if warming has occurred along their path. We measure such changes in arrival time for different travel paths that are sensitive to different parts of the current system, so warming on one side of the current can be distinguished from warming in the other side.

1 Introduction

The heat transfer from the surface to the deep ocean plays an important role in setting the rate at which the Earth warms in response to anthropogenic forcing (e.g., Hansen et al., 1985; Held et al., 2010). Because the Earth's energy imbalance is not well-constrained by radiation measurements at the top of the atmosphere, quantifying this heat transfer requires measurements of both the surface and deep ocean (e.g., Palmer et al., 2011; Trenberth et al., 2014; von Schuckmann et al., 2016; Meyssignac et al., 2019). While the Argo program has provided near-global in situ data from the top 2000 m of the water column since the mid-2000s (e.g., Riser et al., 2016), and repeat hydrography has provided full-depth measurements along a set of transects since the 1990s (e.g., Talley et al., 2016), the spatial and temporal sampling of the existing observing system is too sparse to resolve the mesoscale eddy field, and the associated variance must be treated effectively as a measurement error. This limits our ability to constrain decadal-scale variability and long-term warming, especially in western boundary current regions and the Southern Ocean, where mesoscale eddies are vigorous and associated with mid-depth temperature anomalies of order 1 K.

To complement existing in situ data, Wu et al. (2020), Callies et al. (2023), and Wu et al. (2023) used sound waves generated by natural earthquakes to constrain temperature fluctuations averaged over travel paths that are a few thousand kilometers long (cf., Munk and Wunsch, 1979). These applications of seismic ocean thermometry to the East Indian Ocean revealed qualitative consistency with previous estimates and offered improved constraints on the large-scale variations because local fluctuations are intrinsically averaged along the waves' path. In this paper, we make use of sound waves that are seismically generated off Japan and received at Wake Island, thus sampling the Kuroshio Extension region. We consider a whole set of travel paths from earthquakes along the Japan Trench to Wake Island and invert for large-scale temperature anomaly as a function of the azimuth at which the travel path arrives at Wake Island (Fig. 1). Our approach allows for improved constraints of the large-scale temperature variations in the region reaching back to the 1990s and promises to further insight into the dynamics of the region as well as its response to climate forcing.

The Kuroshio Current separates from the coast around 35°N to form the Kuroshio Extension, a narrow jet associated with a sharp surface and subsurface temperature front marking the boundary between warm subtropical and cold subpolar waters. The current meanders and produces energetic pinched-off mesoscale eddies that evolve on a time

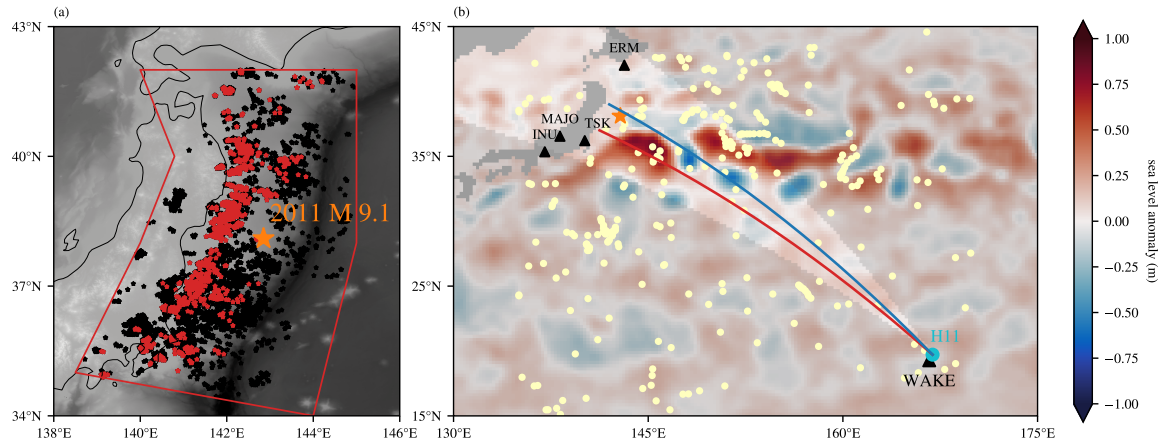

Figure 1: Study area in the Northeast Pacifc. (a) Bathymetry of the Japan Trench and earthquake locations. The red polygon shows the area used in the earthquake search. The black stars are the 7813 ISC catalog earthquakes detected by *P*-wave cross-correlation with a threshold of 0.9 in 1997 to 2021, and the red stars are the repeaters usable for seismic ocean thermometry. The orange star indicates the 2011 M 9.1 Tōhoku earthquake. (b) Sea level anomaly map of the region on 2012-01-01, with the locations of the hydrophone (cyan circle) and seismic stations (black triangles) also shown. The fan that is not grayed out highlights the azimuth range sampled by the *T*-wave paths used in this study. The red and blue curves show great circle paths to H11 at azimuths −1.5° and 1.0° relative to the orange star.

scale of a few tens of days (e.g., Mizuno and White, 1983; Yasuda et al., 1992; Nonaka et al., 2006), and the current switches between straight and meandering paths on a decadal time scale (e.g., Qiu and Chen, 2005). Because of the sharp temperature contrast across the Kuroshio Extension, these dynamics produce large-amplitude temperature variations at a range of length and time scales that are difficult to capture with in situ observations. It is crucial to monitor these transient rearrangements of water masses in order to distinguish them from climate signals consisting of material warming as well as secular rearrangements arising from trends in the circulation.

Western boundary current regions like the Kuroshio Extension region have been suggested to be warming more rapidly than the rest of the global ocean. Wu et al. (2012) estimated from temperature reconstructions that the surface temperature in boundary current regions increased at two to three times the rate of the global mean over the course of the 20th century. Sugimoto et al. (2017) used in situ hydrographic data to

estimate the warming of subtropical mode waters in both the North Pacific and North Atlantic, finding warming rates that were twice as large as at the surface. This accelerated warming of western boundary current regions may be due to a poleward shift or intensification of these currents (Wu et al., 2012; Saba et al., 2016), although the limited record of transport observations for the Gulf Stream since the 1990s shows no evidence of such a trend (Rossby et al., 2019). Considerable uncertainty therefore remains in our understanding of how western boundary current regions respond to the climate forcing, including how deep the warming and suggested transport trends reach.

Seismic ocean thermometry can contribute to better constraints of the large-scale deep-ocean temperature changes of the Kuroshio Extension region. Unlike traditional acoustic tomography methods that require synthetic sound sources, this method uses repeating earthquakes as natural sources of sound waves, so-called *T* waves (Wu et al., 2020). Recent work has explored the use of smaller earthquakes and multi-frequency measurements to improve the time and vertical resolution of the estimates (Wu et al., 2023; Callies et al., 2023). In this study, we use an abundance of repeating earthquakes along the Japan Trench (Igarashi, 2020) to sample the variability of the Kuroshio Extension region arising from current shifts, meanders, and mesoscale eddies. The *T* waves have been received at the CTBTO hydrophone station H11 near Wake Island since 2008. They can also be detected at the WAKE seismic station on the island itself, which provides a digital record reaching back to the 1990s and thus into the pre-Argo era.

The earthquakes used here are spread over a distance of a few hundred kilometers along the Japan Trench (Fig. 1a), a distance that is comparable to the size of the Kuroshio Extension's meanders and the eddies shed by it (Fig. 1b). The travel time of a *T* wave to Wake Island will therefore substantially depend on the back-azimuth. For example, a wave propagating through a string of cold-core eddies will have a very different travel time than a nearby one propagating through a warm anomaly (Fig. 1b). We develop an estimation framework that takes this azimuthal dependence into account. We use maximum likelihood estimation to infer covariance and uncertainty parameters, and we invert for the anomaly field as a function of azimuth and time. Although these estimates are still averages over the travel paths of *T* waves, they clearly exhibit mesoscale signals that are broadly consistent with sea surface elevation data from satellite altimetry, confirming the oceanic origin of the anomalies.

2 Observing *T* waves from repeating earthquakes

We follow a process similar to that described in Wu et al. (2020, 2023) to find repeating earthquakes along the Japan Trench (Fig. 1a). To constrain the search, we restrict source properties in the interactive event catalogue search tool of the International Seismological Centre (ISC) Bulletin. We limit the horizontal location to the polygon shown in Fig. 1a. We limit the source depth to 0 to 100 km, for which the excitation of *T* waves tends to be most efficient. We only use earthquakes with magnitudes M 3.0 to 5.5 as candidates for arrivals at H11 and M 3.5 to 5.5 for arrivals at WAKE because smaller earthquakes generate noisy arrivals, especially at WAKE, and because the source complexity of bigger earthquakes makes repeating signals unlikely. We choose the Japan Meteorological Agency (JMA) as the magnitude author due to its high-quality record. The time coverage is 2007 to 2021 for H11 and 1997 to 2021 for WAKE. These choices result in 51 981 and 27 757 events for H11 and WAKE, respectively. Due to the extensive seismic network on and off Japan, the catalogs are much more complete here than in the study area of Wu et al. (2020, 2023), so no additional earthquake detection needs to be employed.

To identify repeating earthquake pairs and measure the *P*-wave arrival time change to correct the cataloged origin times, we cross-correlate *P* waves at four reference stations MAJO, TSK, ERM, and INU (Fig. 1b). We use seismometers from two location codes at MAJO for better time coverage, yet we exclude duplicate pairs at this station. Similar to the procedure described in Wu et al. (2023), we filter *P* waves using a 1.0 to 3.0 Hz band-pass filter for TSK and a 1.5 to 2.5 Hz band-pass filter for MAJO, TSK, and INU to improve the signal-to-noise ratio (SNR). We set a waveform cross-correlation (CC) coefficient threshold of 0.9 for the detection of *P*-wave repeaters. For a more efficient detection, we only cross-correlate events whose cataloged locations are separated by less than 50 km in the horizontal and vertical and whose magnitude difference is less than 1.5. We further exclude repeating pairs with a *P*-wave arrival time change greater than 15 s, which prevents false detections especially at TSK, where waveforms occasionally show spurious spikes or dense sinusoidal oscillations. This procedure yields 18 632 and 15 836 potential pairs for H11 and WAKE, respectively.

To measure the corresponding *T*-wave arrival time changes, we use H11N3, one of six CTBTO hydrophones present near Wake Island, and seismometers from three location codes at WAKE with duplicate pairs excluded (Fig. 1b). We apply to the received waveforms a Gaussian filter centered on 2.5 Hz and with a width of 0.5 Hz. Compared to the *P*-wave pairs, the corresponding *T*-wave pairs show reduced waveform correlation.

Wu et al. (2020, 2023) ascribed a similar reduction in the East Indian Ocean to source complexity and a changing ocean sound speed field between repeating events, both of which might be important for the Kuroshio measurements as well. The *T*-wave excitation is understood to be confined to a narrow section of the trench, maybe a few tens of kilometers wide (de Groot-Hedlin and Orcutt, 1999; Okal, 2008). Horizontal and vertical refraction by sound speed anomalies due to mesoscale eddies and other transients (e.g., Munk, 1980; Dushaw, 2014) could change the waveforms between repeating events. Interaction with bathymetry, especially the numerous tall seamounts in the region, can further induce mode coupling and reduce the SNR and CC. As in previous work, we set a CC threshold of 0.6 for the *T*-wave pairs.

Furthermore, because the energetic Kuroshio Current system produces large *T*-wave travel time anomalies, cycle skipping is common in the CC measurements. We apply the correction described in Callies et al. (2023), using measurements at 3.5 Hz with a CC threshold of 0.3 to calculate differential delays. We extend this correction approach by also allowing for double cycle skips. The correction detects pairs experiencing cycle skips that arise from the dispersive nature of *T* wave (Callies et al., 2023). The correction procedure also depends on the Bayesian inversion framework to be introduced in the next section.

We additionally exclude a few spurious pairs manually. These pairs may be false detections, suffer from timing errors, or experience three or more cycle skip. We identify these spurious pairs by examining outliers in inversion residuals, cycle-skipping correction clusters, and scatter plots comparing data from H11, WAKE, and altimetry. We exclude a total of 16 and 40 pairs for H11 and WAKE, respectively. This results in a remaining 1566 and 1201 *T*-wave repeaters for H11 and WAKE, respectively, a great reduction in number from their detectable *P*-wave counterparts. As in the Indian Ocean application, compared with the land station, the hydrophone helps detect more repeaters by having a better SNR for small earthquakes ($M < 4.0$). For larger earthquakes, the detection rates are similar between H11 and WAKE (Fig. 2a).

3 Inferring anomalies in azimuth and time

Each repeating earthquake pair that passes our selection criteria supplies measurements of one *T*-wave arrival time change and one to four *P*-wave arrival time changes. We interpret the *P*-wave arrival time changes as arising from errors in the cataloged event times and refer to the difference between the *T*- and *P*-wave arrival time changes as "*T*-

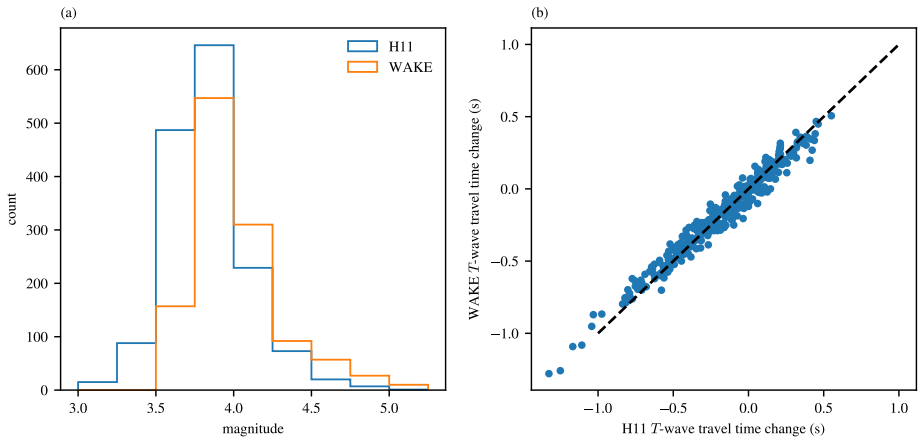

Figure 2: Usable repeating earthquakes and observed T-wave travel time changes. (a) Histogram of the magnitudes of repeaters detected at H11 (total of 1566 pairs) and WAKE (total of 1201 pairs). (b) Origin-time corrected T-wave travel time changes at WAKE vs. H11 for the 363 common repeaters (blue dots). The one-to-one line is shown in black dashed.

wave travel time changes". We ascribe all change in the T-wave travel time to changes in the ocean's sound speed between the repeating events and further assume that these sound speed changes are dominated by temperature changes, neglecting much smaller contributions from salinity anomalies and currents (Wu et al., 2020). The T-wave travel anomalies then correspond to kernel-weighted temperature anomalies along travel path between the two events, i.e., the travel time anomaly τ as a function of azimuth α and time t is

$$\tau(\alpha, t) = \iint K(\alpha, r, z)\, T(\alpha, r, z, t)\, \mathrm{d}r\, \mathrm{d}z, \tag{1}$$

where K is the sensitivity kernel that can be calculated using SPECFEM2D (cf., Wu et al., 2020) and T is the temperature anomaly field. We assume the sensitivity is confined to the great-circle path, so the integration is in range r and depth z only.

Each usable repeater thus provides a constraint on the time- and azimuth-dependent kernel-weighted temperature anomaly that we would like to infer—but it constrains only its *change* between the event times. To invert for the anomalies themselves, we model the anomaly field as a stationary Gaussian process in time and azimuth, impose a set of prior and noise statistics, and calculate the Gaussian posterior mean and covariance (e.g., Kaipio and Somersalo, 2005; Wunsch, 2006; Sanz-Alonso et al., 2023). Here, a Gaussian process refers to a random function whose values at any finite set of time–azimuth points

follow a multivariate Gaussian distribution.

3.1 Formulating the linear inverse problem

To formulate the linear inverse problem, we relate the measurements of T- and P-wave arrival time change $\boldsymbol{\delta}_\mathrm{T}$ and $\boldsymbol{\delta}_\mathrm{P}$ between repeating earthquakes to the T- and P-wave arrival time anomalies $\boldsymbol{a}_\mathrm{T}$ and $\boldsymbol{a}_\mathrm{P}$ at all event times and azimuths involved in a measurement:

$$\boldsymbol{\delta} = \mathbf{E}\boldsymbol{a} + \boldsymbol{n} \quad \text{with} \quad \boldsymbol{\delta} = \begin{pmatrix} \boldsymbol{\delta}_\mathrm{T} \\ \boldsymbol{\delta}_\mathrm{P} \end{pmatrix}, \quad \mathbf{E} = \begin{pmatrix} \mathbf{X}_\mathrm{T} & \mathbf{0} & \mathbf{A} \\ \mathbf{0} & \mathbf{X}_\mathrm{P} & \mathbf{0} \end{pmatrix}, \quad \boldsymbol{a} = \begin{pmatrix} \boldsymbol{a}_\mathrm{T} \\ \boldsymbol{a}_\mathrm{P} \\ \boldsymbol{a}_\mathrm{fit} \end{pmatrix}, \quad \boldsymbol{n} = \begin{pmatrix} \boldsymbol{n}_\mathrm{T} \\ \boldsymbol{n}_\mathrm{P} \end{pmatrix}. \quad (2)$$

The solution vector $\boldsymbol{a}$ contains the T- and P-wave arrival time anomalies as well contributions to the T-wave travel time anomalies from a linear trend as well as annual and semi-annual cycles, represented by $\boldsymbol{a}_\mathrm{fit}$. We ignore azimuthal dependencies in the linear trend and the seasonal cycle based on sea level anomaly calculation (details in the next subsection), in which their azimuthal gradients are negligible compared with large-scale averages. The design matrix $\mathbf{E}$ consists of the pair matrices $\mathbf{X}_\mathrm{T}$ and $\mathbf{X}_\mathrm{P}$ that take differences between the events involved in each measurement and the matrix $\mathbf{A}$ that takes differences between the signals that arise from the linear trend and seasonal signals. Callies et al. (2023) described how these matrices are constructed. Contributions to the measurement errors $\boldsymbol{n}$ will be discussed below.

The T-wave travel time anomalies are obtained by taking the difference between the T- and P-wave arrival time anomalies: $\boldsymbol{\tau} = \mathbf{D}\boldsymbol{a}$, where $\mathbf{D}$ is the difference matrix as defined in Callies et al. (2023). We convert these travel time anomalies to kernel-weighted temperature anomalies $\langle \boldsymbol{T} \rangle = K_\mathrm{B}\boldsymbol{\tau}$ using the bulk sensitivity $K_\mathrm{B} = \iint K \, \mathrm{d}r \, \mathrm{d}z$. We calculate kernels for H11 and WAKE using two source locations separated by 3° in azimuth (141.25°E, 37.00°N and 142.00°E, 39.00°N). These calculations give $K_\mathrm{B} = -6.03$ and -6.18 K s^{-1} for H11 and $K_\mathrm{B} = -5.96$ and -5.98 K s^{-1} for WAKE. The azimuthal dependence of the bulk sensitivity thus appears to be weak, and we use $K_\mathrm{B} = -6$ K s^{-1} throughout. We also exclude any uncertainties associated with this conversion from the uncertainty estimates discussed below.

The sensitivity kernels tend to peak around 1.5 km depth for both receivers (Fig. 3). This is similar to kernels used in Wu et al. (2020), Callies et al. (2023), and Wu et al. (2023). There are some differences between the kernels for H11 and WAKE. The kernels for H11 are fairly homogeneous in range and appear to consist primarily of the fundamental acoustic mode (Fig. 3ac). The kernels for WAKE, in contrast, exhibit range depen-

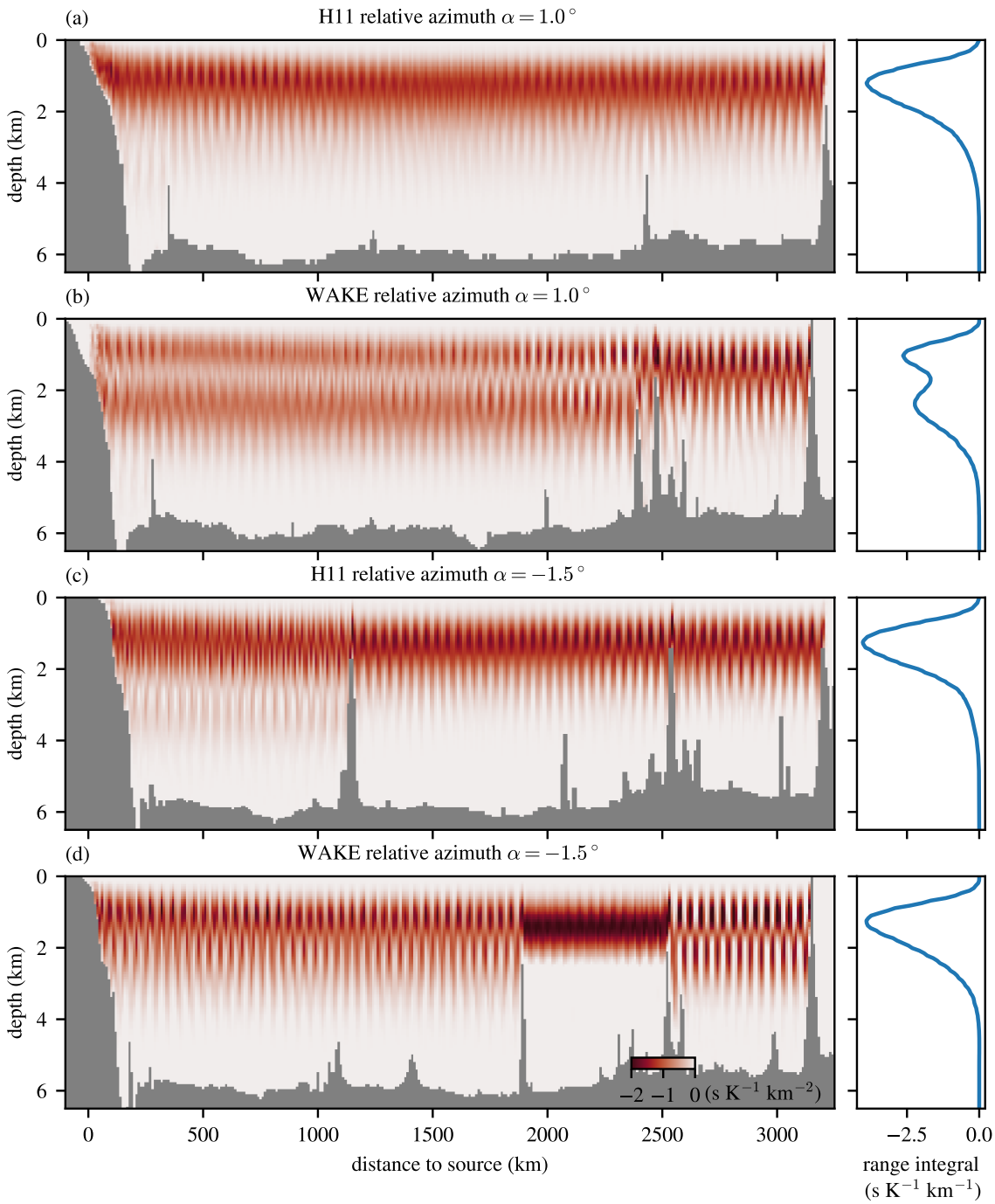

Figure 3: *T*-wave sensitivity kernels at the sampling frequency 2.5 Hz from SPECFEM2D numerical simulation. (a,c) Kernels at azimuths $\alpha = 1.0^\circ$ and -1.5° referenced at H11. (b,d) Kernels at the same azimuths referenced at WAKE. Left panels show range-dependent kernels, and right panels show corresponding range integrals.

dence due to interaction with bathymetry (Fig. 3b,d). In particular, at azimuth $\alpha = -1.5°$ two seamounts constrain the sensitivity to above 2 km depth between about 2000 and 2500 km from the source, while at azimuth $\alpha = 1.0°$ a group of adjacent seamounts generate complex mode interactions and induce higher-order mode energy within 2500 km from the source. These differences highlight the importance of the bathymetry near the receivers and suggest that *T* waves received at H11 and WAKE sample different waters even at the same azimuth. It should be noted, however, that three-dimensional propagation effects neglected in the kernel calculations might change the details of the kernels' structure. As discussed below, the two receivers produce very similar travel time anomalies, so we neglect the azimuth dependence of the sensitivity kernels and the ways this would affect covariances of *T*-wave travel time anomalies.

3.2 Constructing prior and noise covariance models

We specify the prior statistics for *T*-wave travel time anomalies with a correlation structure in both time and azimuth, and we improve on the simple noise covariances used in Wu et al. (2020), Callies et al. (2023), and Wu et al. (2023) to better model source location discrepancy and hydrophone motion in addition to measurement errors arising from noisy waveforms. Furthermore, we employ maximum likelihood estimation to infer the parameters of our covariance model from the data themselves.

We prescribe a time–azimuth covariance function based on range-averaged sea level anomaly inferred from satellite altimetry. While seismic thermometry and satellite altimetry measure different ocean properties—*T* waves sample the ocean's sound speed with sensitivities peaking at mid-depth, whereas altimetry measures the sea level change due to thermal expansion, haline expansion, and mass variation (e.g., Wunsch and Stammer, 1998)—they have in common that they are sensitive to Kuroshio Extension meanders and mesoscale eddies. The range-averaged sea level anomaly substantially differs from the *T*-wave signal in that it includes a strong seasonal signal arising from the seasonal warming and cooling of the surface ocean (Gill and Niiler, 1973), which is absent in the *T*-wave data because *T* waves have little sensitivity near the surface (Fig. 3). Once this seasonal signal is removed, the range-averaged sea level and *T* signals covary significantly, and the altimetry data can be used to estimate the azimuth and time covariance structure of *T*-wave travel time anomalies.

Specifically, we use the sea level daily gridded data from satellite observations available at the Copernicus Climate Change Service Climate Data Store. We use the data from

2010 to 2019 at the 1st, 6th, 11th, 16th, 21st, and 26th day of each month and linearly interpolate the anomaly field onto a range of great circle paths from Japan Trench to Wake Island. These paths have a horizontal resolution of 10 km and represent T-wave trajectories with various azimuths. The northwestward direction of each path points to 142.86°E and a latitude varying from 33 to 43°N with a resolution of 0.1°. Along each path, we range-average the interpolated anomaly to get a time series for the corresponding azimuth, analogous to how T waves sample the path. We fit to each time series a function consisting of a mean, a linear trend, an annual sinusoid, and a semi-annual sinusoid. We then subtract these fits from the original time series. To calculate the time–azimuth covariance, we subset the result into five overlapped five-year chunks with the first year ranging from 2010 to 2015. We then interpolate each chunk onto a regular grid with five-day time resolution and 0.3° azimuth resolution and calculate the two-dimensional power spectrum, averaging over the five chunks. We inverse-transform the power spectrum to get an estimate of the covariance function.

The covariance of these range-averaged sea level anomalies is well-captured by a product between an exponential decay in time and a Gaussian decay in azimuth. Therefore, we assume a stationary and separable time–azimuth covariance function for the stochastic part of the T-wave travel time anomalies: the covariance between times t_i and t_j and azimuths α_i and α_j is

$$C_{ij} = \sigma_\tau^2 \exp\left[-\frac{|t_i - t_j|}{\lambda_\mathrm{t}} - \frac{(\alpha_i - \alpha_j)^2}{2\lambda_\alpha^2}\right], \tag{3}$$

where λ_t and λ_α determine the correlation scale in time and azimuth, respectively. The deterministic parts of the T-wave travel time anomalies—the linear trend, an annual cycle, and a semi-annual cycle—are assumed mutually independent and independent of the stochastic part. Their prior covariance is prescribed through a diagonal matrix $\boldsymbol{\Xi}$, and the prior standard deviations are set to $\sigma_\mathrm{t} = 0.01$ s yr^{-1} for the trend (corresponding to 1.7 mK yr^{-1}) and $\sigma_\mathrm{a} = \sigma_\mathrm{sa} = 0.1$ s for the seasonal cycle.

We assign these covariances of the T-wave travel time anomalies to the T-wave arrival time anomalies $\boldsymbol{a}_\mathrm{T}$. The T-wave arrival time anomalies $\boldsymbol{a}_\mathrm{T}$ also contain the errors in the cataloged event times that we constrain with the P-wave arrival time anomalies $\boldsymbol{a}_\mathrm{P}$. We thus prescribe the covariance matrix for the stacked vector $\boldsymbol{a}$ as

$$\mathbf{R} = \begin{pmatrix} \mathbf{C} & \mathbf{0} & \mathbf{0} \\ \mathbf{0} & \mathbf{0} & \mathbf{0} \\ \mathbf{0} & \mathbf{0} & \boldsymbol{\Xi} \end{pmatrix} + \sigma_\mathrm{o}^2 \begin{pmatrix} \mathbf{I} & \mathbf{I} & \mathbf{0} \\ \mathbf{I} & \mathbf{I} & \mathbf{0} \\ \mathbf{0} & \mathbf{0} & \mathbf{0} \end{pmatrix}, \tag{4}$$

where σ_{o} is the prior standard deviation of the *P*-wave arrival time anomalies. The *T*- and *P*-wave arrival time anomalies arising from these origin time corrections are the same and thus perfectly correlated.

For the measurement error $\boldsymbol{n}$, we assume that it arises from four distinct processes: a discrepancy in the source location of the repeating earthquakes, a difference in the hydrophone location between the two events (for H11 only), and the errors arising from the correlation of noisy *P* and *T* waveforms. The location uncertainties are given in terms of corresponding travel time anomalies. We assign different errors for the latter two because the *P* and *T* waveforms arise from distinct propagation processes, instrumentation, and data processing. We further assume these four components to be independent and the underlying anomalies to be zero-mean Gaussian random variables. We assign isotropic source and hydrophone location uncertainties and specify the noise statistics

$$\mathbf{N} = \sigma_{\mathrm{s}}^2 \left(\mathbf{E}_{\cos} \mathbf{E}_{\cos}^{\mathrm{T}} + \mathbf{E}_{\sin} \mathbf{E}_{\sin}^{\mathrm{T}} \right) + \sigma_{\mathrm{h}}^2 \left(\mathbf{E}_{T,\cos} \mathbf{E}_{T,\cos}^{\mathrm{T}} + \mathbf{E}_{T,\sin} \mathbf{E}_{T,\sin}^{\mathrm{T}} \right) + \sigma_{\eta}^2 \mathbf{I}_{\mathrm{T}} + \sigma_{\varepsilon}^2 \mathbf{I}_{\mathrm{P}}, \tag{5}$$

where σ_{s}^2 is the variance of the source location discrepancy, σ_{h}^2 the hydrophone location variance, σ_{η}^2 the measurement noise variance for *T* waves, and σ_{ε}^2 the measurement noise variance for *P* waves. The source and hydrophone location error variances are not diagonal and specified using

$$\mathbf{E}_{\cos} = \begin{pmatrix} \mathbf{X}_{\mathrm{T},\cos} \\ \mathbf{X}_{\mathrm{P},\cos} \end{pmatrix}, \quad \mathbf{E}_{\sin} = \begin{pmatrix} \mathbf{X}_{\mathrm{T},\sin} \\ \mathbf{X}_{\mathrm{P},\sin} \end{pmatrix}, \quad \mathbf{E}_{T,\cos} = \begin{pmatrix} \mathbf{X}_{\mathrm{T},\cos} \\ \mathbf{0} \end{pmatrix}, \quad \mathbf{E}_{T,\sin} = \begin{pmatrix} \mathbf{X}_{\mathrm{T},\sin} \\ \mathbf{0} \end{pmatrix}. \tag{6}$$

These matrices consist of trigonometric pair matrices obtained by replacing ± 1 in $\mathbf{X}_{\mathrm{T}}$ and $\mathbf{X}_{\mathrm{P}}$ with $\pm \cos\theta_i$ or $\pm \sin\theta_i$, where θ_i is the azimuth of the event pair i, calculated from the average catalog location of the two events. The hydrophone movement due to local currents is generally expected to be complicated and anisotropic (Nichols and Bradley, 2017), yet the representation as an isotropic Gaussian displacement used here should be a reasonable first step to account for this uncertainty. The diagonal matrices $\mathbf{I}_{\mathrm{T}}$ and $\mathbf{I}_{\mathrm{P}}$ contain identity sub-matrices for *T*- and *P*-wave data, respectively, such that $\mathbf{I} = \mathbf{I}_{\mathrm{T}} + \mathbf{I}_{\mathrm{P}}$. For WAKE data, we set $\sigma_{\mathrm{h}} = 0$. All together, the observed arrival time change vector $\boldsymbol{\delta}$ is assumed to be a Gaussian variable with zero mean and covariance $\boldsymbol{\Sigma} = \mathbf{ERE}^{\mathrm{T}} + \mathbf{N}$.

3.3 Estimating prior variances, correlation scales, and error variances

Within the formulation above, the measurement covariance matrix $\boldsymbol{\Sigma}$ is a function of the parameters

$$\boldsymbol{\theta} = (\lambda_{\mathrm{t}}, \lambda_{\alpha}, \sigma_{\tau}, \sigma_{\mathrm{o}}, \sigma_{\mathrm{s}}, \sigma_{\mathrm{h}}, \sigma_{\eta}, \sigma_{\varepsilon}), \tag{7}$$

and the log-likelihood of $\boldsymbol{\theta}$ is

$$\mathscr{L}(\boldsymbol{\theta}) = \log p(\boldsymbol{\delta}|\boldsymbol{\theta}) = -\frac{1}{2}\left(\log\det\boldsymbol{\Sigma} + \boldsymbol{\delta}^{\mathrm{T}}\boldsymbol{\Sigma}^{-1}\boldsymbol{\delta} + n\log 2\pi\right), \tag{8}$$

where n is the length of the observation vector $\boldsymbol{\delta}$. We do not aim to estimate the variances of the linear trend and seasonality and exclude them from the parameter vector $\boldsymbol{\theta}$ because the data supply but one realization and therefore provide a weak constraint. The maximum likelihood estimator (MLE) of $\boldsymbol{\theta}$ is

$$\hat{\boldsymbol{\theta}} = \underset{\boldsymbol{\theta}\in\mathbb{R}^7}{\arg\max}\,\mathscr{L}(\boldsymbol{\theta}) = \underset{\boldsymbol{\theta}\in\mathbb{R}^8}{\arg\min}\left(\log\det\boldsymbol{\Sigma} + \boldsymbol{\delta}^{\mathrm{T}}\boldsymbol{\Sigma}^{-1}\boldsymbol{\delta}\right). \tag{9}$$

To obtain the MLE via numerical optimization, we log-transform the parameters, which must all be positive, and use the BFGS quasi-Newton algorithm with a line search satisfying the strong Wolfe conditions (Nocedal and Write, 2006). We further examine the marginal distribution for each parameter around the MLE, and we compare the results between H11 and WAKE, both for the full population of repeating pairs and for the restricted population of 363 pairs that yield a successful measurement at both receivers. We expect the correlation scales λ_{t} and λ_{α} to be comparable to the corresponding scales in the range-averaged sea level anomalies, which gives 71 days in time and 1.6° in azimuth.

The MLE using pairs detected at both receivers produces mutually consistent estimates that align with expectations (Fig. 4, dashed lines). The distributions for the time correlation scale λ_{t} from both receivers peak at 60 days, which is in line with typical time scales of the Kuroshio Extension meanders and mesoscale eddies. The distributions for the azimuth correlation scale λ_{α} center around 2.2°, which is slightly greater than that inferred from the sea level anomaly covariance, likely due to distributed T-wave excitation. The standard deviation scale σ_{τ} for the stochastic part of the travel time anomalies is 0.28 s, equivalent to a temperature anomaly scale of 47 mK.

The two receivers give indistinguishable distributions for the standard deviation σ_{o} of the P-wave arrival time anomalies that peak at 0.88 s, consistent with the general timing uncertainty of seismic events. The measurement error σ_{η} is 6.8 ms for WAKE and H11, greater than that arising from P-wave correlation at 3.2 ms. The distribution for the source location discrepancy σ_{s} peaks at 13 ms, equivalent to a distance on the order of 100 m. The hydrophone data further suggests a receiver location uncertainty σ_{h} of 11 ms, equivalent to a distance of 17 m. The broad distribution could implies that this error is not well-constrained by just common pairs, which likely contributes to a larger waveform correlation error at H11.

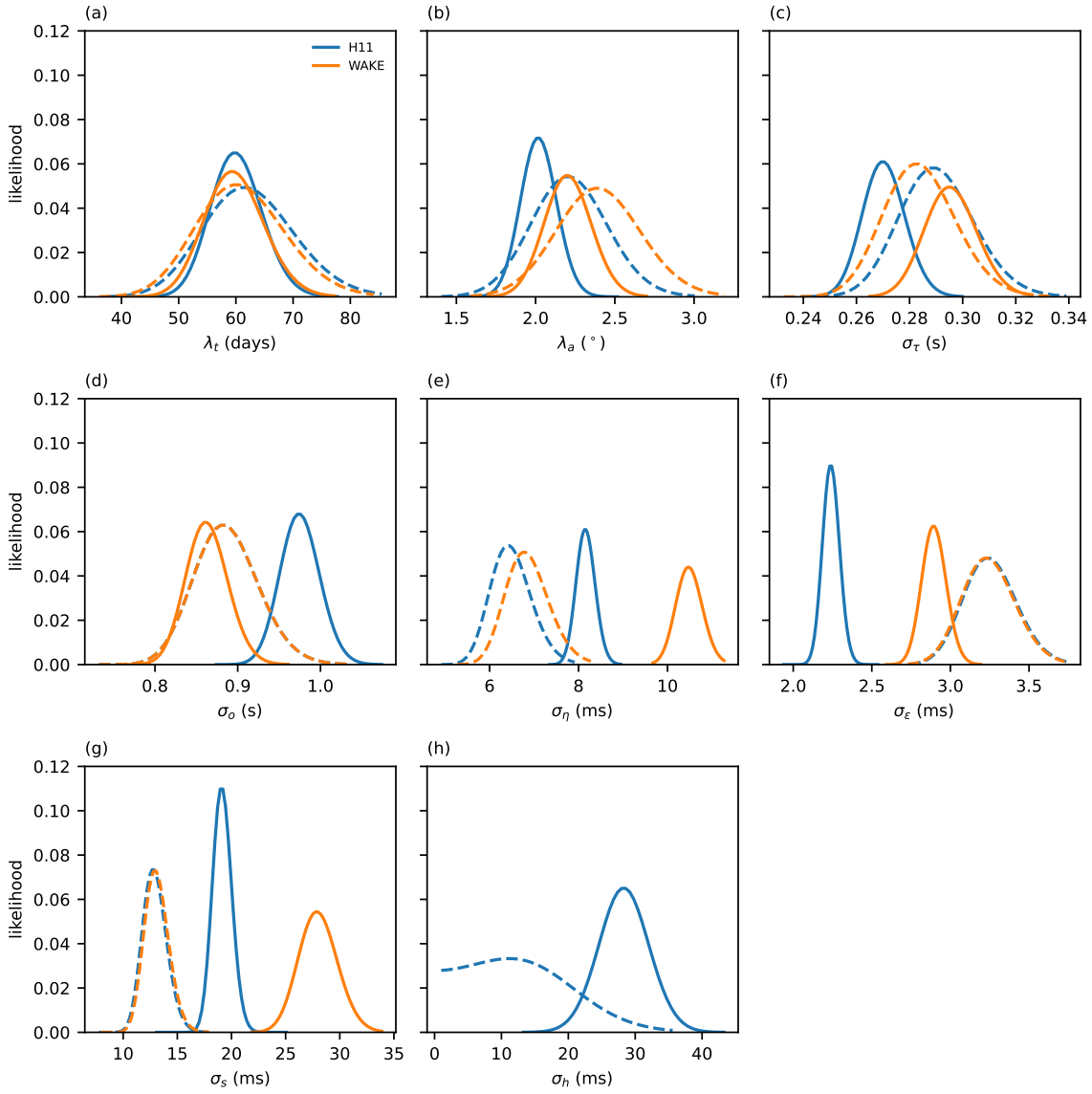

Figure 4: Marginal likelihood distributions for H11 (blue) and WAKE (orange). Shown are (a) time correlation scale. (b) azimuth correlation scale. (c) travel time anomaly scale. (d) origin time deviation scale (dashed lines indistinguishable), (e) *T*-wave instrumental uncertainty, (f) *P*-wave instrumental uncertainty, (g) source location discrepancy and (h) hydrophone location uncertainty. Each distribution consists of 50 weighted sample points such that the result is independent of resolution. To calculate the distribution, we independently vary the corresponding parameter around its MLE result while keep other parameters fixed. Dashed and solid lines show distributions using common pairs only and full catalogs, respectively.

The source location discrepancy distribution provides a quantitative constraint on the T-wave source properties. It demonstrates directly that the uncertainty arising from differences in the source locations of the repeating events is an order of magnitude smaller than the signal arising from temperature changes in the ocean. This result is consistent with the analysis in the supplementary material of Wu et al. (2020). Compared with the noise statistics formulation of Wu et al. (2020), Callies et al. (2023), and Wu et al. (2023), incorporating this effect explicitly reduces the overall uncertainty of the inferred temperature signal. We can also generalize the location covariance to include discrepancies in the depth as well as anisotropy, but we leave this refinement to future work.

Compared to the MLE using only common pairs, estimates with full catalogs of the two receivers tend to be better constrained but also exhibit more pronounced differences between the two receivers (Fig. 4 solid lines, Table 1). The three parameters characterizing the oceanic variability, the time and azimuth correlation scales λ_t and λ_α as well as the T-wave travel time anomaly scale σ_τ have distributions that substantially overlap, both between the two receivers and with the common-catalog estimates. The correlation constants stay around 60 days and 2.0°.

The full-catalog estimate for the origin time correction σ_o is larger for H11, while that for WAKE mostly overlaps with the common-catalog estimate (Fig. 4d). This is likely because the smaller earthquakes detected at H11 tend to have larger errors in the cataloged origin time.

The full-catalog T-waveform correlation error σ_η is estimated to be significantly larger for WAKE than for H11, and both estimates are significantly larger than their common-catalog estimates (Fig. 4e). We can understand this error increase as arising from a modest drop in the coherence between waveforms. Both receivers have a mean CC of 0.75 for the common repeaters, but this drops to 0.71 and 0.72 at H11 and WAKE, respectively, when using the full catalog. The differences in travel time changes inferred from the two receivers generally increases as the CC drops, implying that a coherence reduction generally translates into an increased correlation error σ_η. Interestingly, the coherence reduction for a given pair is distinct at the two receivers. In addition to the 363 common repeaters, H11 detects 898 repeaters that do not pass the CC > 0.6 threshold at WAKE, while WAKE detects another 605 repeaters that do not pass the threshold at H11. If the generally lower SNR at WAKE was the main cause for coherence reduction, most pairs detected at WAKE would also be detected at H11. Similarly, if changes in the source properties dominated the coherence loss, the coherence drop should be similar at the two receivers. We therefore suspect that the coherence loss is instead dominated by changes

to the waveforms caused by strong ocean perturbation coupled with differences in the sensitivity along the two paths (Fig. 3). As a result, for any given pair, one receiver might suffer a coherence drop beyond the threshold when the other suffers a smaller drop that merely leads to an increase in the correlation error σ_η. That said, the higher noise in the waveforms from small earthquakes detected at H11 only likely also contribute to the increased error.

In contrast, the *P*-waveform correlation error σ_ε is reduced in the full catalogs, significantly so for H11 (Fig. 4f). The partition of measurements among the four *P*-wave stations could matter. INU and ERM detect smaller earthquakes than MAJO and TSK but have worse SNR statistics when averaged over all detections. INU and ERM measurements make up 26.7 %, 29.0 %, and 28.5 % of all measurements for H11, WAKE, and the common catalog, respectively, so the H11 catalog has a larger contribution from the more reliable reference stations MAJO and TSK. Another possible explanation for the drop in the correlation error is that the events detected as repeaters in the full catalogs are more ideally located for good measurements on the *P*-wave stations. For example, the full catalog includes 51 pairs north of 40°N that are close to ERM station, whereas the common catalog only has one of them.

The reduction in *P*-waveform correlation error goes along with a significant increase in the source location error σ_o (Fig. 4g). This could be because detecting coherent waveforms at both receivers puts a more stringent constraint on the source location properties of the repeating events.

The most likely hydrophone location error σ_h increases for H11 compared to the common-pair catalog (Fig. 4h). The distribution inferred from the common-pair catalog is fairly broad, however, and overlaps substantially with that inferred from the full H11 pair catalog.

Given this discussion, it seems reasonable to use the parameters inferred from the full catalogs in the inversion for *T*-wave travel time anomalies (Table 1). The noise characteristics are then a better representation of the noise present in the respective catalogs used, while the physical parameters are very close to one another for the two stations.

3.4 Inverting for posterior distribution

Given covariances with parameters inferred using maximum likelihood estimation (Table 1), we solve for the mean $\tilde{\boldsymbol{a}}$ and covariance $\mathbf{P}$ of the Gaussian posterior:

$$\tilde{\boldsymbol{a}} = \mathbf{P}\mathbf{E}^{\mathrm{T}}\mathbf{N}^{-1}\boldsymbol{\delta} \quad \text{and} \quad \mathbf{P} = \left(\mathbf{R}^{-1} + \mathbf{E}^{\mathrm{T}}\mathbf{N}^{-1}\mathbf{E}\right)^{-1}. \tag{10}$$

	λ_t (days)	λ_α (°)	σ_τ (s)	σ_o (s)	σ_s (ms)	σ_h (ms)	σ_η (ms)	σ_ε (ms)
H11	60	2.0	0.27	0.97	19	28	8.1	2.2
WAKE	59	2.2	0.29	0.86	28	–	10	2.9

Table 1: Parameters used for the time series inversion for H11 and WAKE. The parameter values are inferred using maximum likelihood estimation from the full set of repeating earthquakes detected by the respective receiver.

We can obtain the posterior mean of the *T*-wave travel time anomaly vector $\boldsymbol{\tau}$ as $\tilde{\boldsymbol{\tau}} = \mathbf{D}\tilde{\boldsymbol{a}}$, and the corresponding posterior covariance is $\mathbf{DPD}^{\mathrm{T}}$.

With the same prior statistics, we can formulate another inverse problem to interpolate these irregular samples of the anomaly field onto a regular time–azimuth grid. We use a grid resolution of 10 days and 0.25°, and we calculate estimates for azimuths between ±9°. We estimate the arrival time anomalies at the grid points $\boldsymbol{a}_g$, which as before also includes the fit parameters $\boldsymbol{a}_{\mathrm{fit}}$, for one year at a time:

$$\tilde{\boldsymbol{a}}_g = \mathbf{R}_{ga}\mathbf{R}^{-1}\tilde{\boldsymbol{a}} = \mathbf{R}_{ga}\mathbf{E}^{\mathrm{T}}\boldsymbol{\Sigma}^{-1}\boldsymbol{\delta}, \tag{11}$$

where $\mathbf{R}_{ga}$ is the prior covariance between $\boldsymbol{a}_g$ and $\boldsymbol{a}$. The gridded travel time anomalies are then inferred as $\boldsymbol{\tau}_g = \mathbf{D}_g\tilde{\boldsymbol{a}}_g$, where $\mathbf{D}_g$ is like $\mathbf{D}$ except that it acts on the gridded arrival time anomalies. The posterior covariance of the gridded travel time anomalies is then $\mathbf{D}_g(\mathbf{R}_{gg} - \mathbf{R}_{ga}\mathbf{E}^{\mathrm{T}}\boldsymbol{\Sigma}^{-1}\mathbf{E}\mathbf{R}_{ga}^{\mathrm{T}})\mathbf{D}_g^{\mathrm{T}}$, where $\mathbf{R}_{gg}$ is the prior covariance matrix for $\boldsymbol{a}_g$. We estimate the corresponding range-averaged temperature anomalies using the bulk sensitivity, $\langle\tilde{\boldsymbol{T}}_g\rangle = K_B\tilde{\boldsymbol{\tau}}_g$, and scale the uncertainty accordingly.

3.5 Cycle-skipping correction

The cycle-skipping correction performs a cluster analysis based on Gaussian mixture models and the inversion statistics. It analyzes *T*-wave pairs in a scatter plot comparing the differential *T*-wave travel time anomaly between 3.5 and 2.5 Hz with the travel time anomaly at 2.5 Hz. The former can be calculated directly from the data, whereas the latter requires the subtraction of the *P*-wave arrival time anomaly, so we use $\boldsymbol{\delta}_{\mathrm{T}} - \mathbf{X}_{\mathrm{T}}\tilde{\boldsymbol{a}}_{\mathrm{P}}$. The analysis uses a Gaussian mixture model with four (for H11) and five (for WAKE) members and shared covariance to find clusters of pairs. We perform an initial cycle-skipping correction based on the identified cluster. We then cycle through the *T*-wave pairs to find additional corrections (or reverse initial corrections) that reduce negative

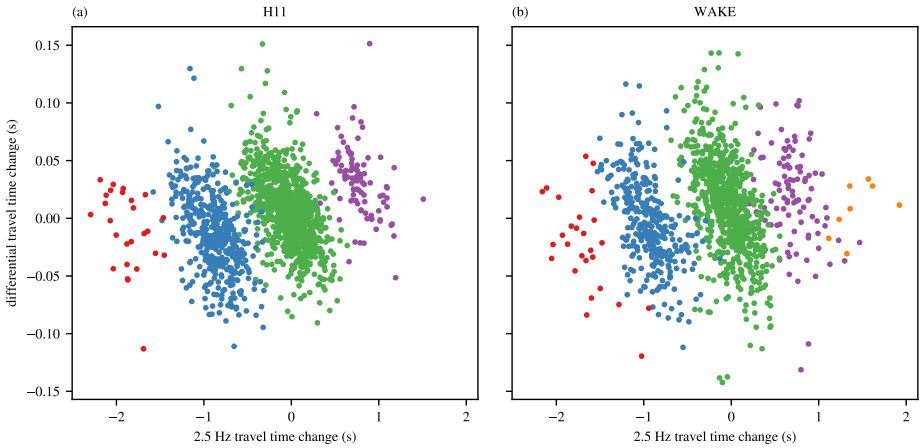

Figure 5: Cycle-skipping corrections for the data received at (a) H11 and (b) WAKE. Shown are the differential *T*-wave travel time changes between 3.5 and 2.5 Hz vs. the corresponding travel time changes at 2.5 Hz. The red and blue dots indicate pairs for which cycle skipping is corrected to the right, the purple and orange dots indicate pairs for which cycle skipping is corrected to the left, and the green dots indicate pairs for which no cycle-skipping correction is made.

log-likelihood until no further corrections are found. The details of the algorithm are discussed in Callies et al. (2023). To finalize the pair catalog, we iterate between the MLE and cycle-skipping corrections to exclude a few outliers until the MLE does not change with further corrections.

For H11 and WAKE, this procedure corrects about 2 % of the pairs to the right twice, 28 % of the pairs to the right once, and 6 % of the pairs to the left once (Fig. 5). For WAKE, a few pairs are also corrected to the left twice (Fig. 5b). The fraction of pairs affected by cycle skipping is greater than in the East Indian Ocean (Wu et al., 2020; Callies et al., 2023; Wu et al., 2023) because travel time anomalies tend to be larger in the Kuroshio Extension region, making cycle skipping more likely.

3.6 Testing prior assumptions

An essential step for implementing the inversion is testing the prior assumptions (e.g., Wunsch, 2006; Kuusela and Stein, 2018). We confirm that our prior covariances are a reasonable choice by comparing predictions based on the inversion with measurements from the population of pairs detected at both H11 and WAKE (Fig. 6). For each pair in that population, we use the remaining pairs and a Gaussian process regression to predict the

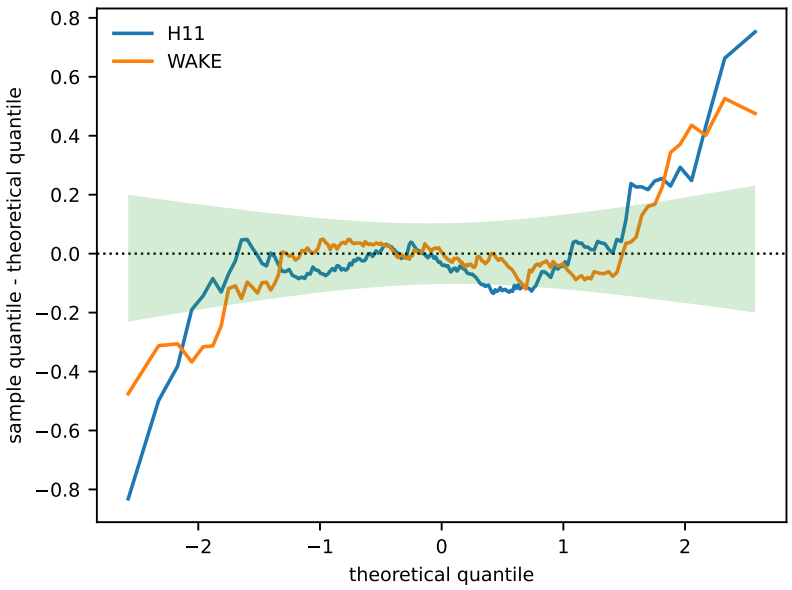

Figure 6: Difference between the sample quantile and the corresponding standard Gaussian theoretical quantile ($q_{\text{sample}} - q_{\text{theory}}$) plotted against the theoretical quantile (q_{theory}) for the leave-one-out cross-validation using the 363 pairs detected at both H11 and WAKE. Shown are quantile differences using H11 data (blue) and WAKE data (orange) as well as a two-sided 95 % confidence interval (light green).

measurement for this left-out pair. Specifically, the predictive mean $\hat{m}_{-i}$ and variance $\hat{v}_{-i}$ for the ith arrival time change δ_i are

$$\hat{m}_{-i} = \mathbf{R}_i^{\mathrm{T}} \boldsymbol{\Sigma}_{-i}^{-1} \boldsymbol{\delta}_{-i} \quad \text{and} \quad \hat{v}_{-i} = \boldsymbol{\Sigma}_{ii} - \mathbf{R}_i^{\mathrm{T}} \boldsymbol{\Sigma}_{-i}^{-1} \mathbf{R}_i, \tag{12}$$

where $\mathbf{R}_i = \boldsymbol{\Sigma}_i - \sigma_\eta^2 \boldsymbol{e}_i$ is the covariance vector between δ_i and the remaining measurements, $\boldsymbol{e}_i$ the unit vector along the ith dimension, $\boldsymbol{\Sigma}_{-i}$ and $\boldsymbol{\delta}_{-i}$ the pre-defined data covariance and vector with the appropriate entries removed, and $\boldsymbol{\Sigma}_{ii}$ the ith diagonal of $\boldsymbol{\Sigma}$. We use parameters from the MLE for the full set of pairs detected at both H11 and WAKE. If the covariance prescription is consistent with the data, it follows that the random variable $(\delta_i - \hat{m}_{-i})/\sqrt{\hat{v}_{-i}}$ is standard Gaussian. Therefore, we can compare the normalized sample quantiles of $\{(\delta_i - \hat{m}_{-i})/\sqrt{\hat{v}_{-i}}, i = 1, \ldots, 352\}$ with the theoretical standard Gaussian quantile.

For both H11 and WAKE, the center of the distribution is close to Gaussian, but the tails are markedly heavy (Fig. 6). This is not too surprising, given the complexity of the ocean signal sampled here, arising from strongly nonlinear and thus non-Gaussian

Kuroshio Extension meanders and mesoscale eddies, contrasted with the relative simplicity of our statistical model. The heavy tails are reassuring insofar as they indicate that the CC threshold and outlier rejection does not lead to a sample that is strongly biased toward small anomalies. Non-stationarity, especially in azimuth, is another possible explanation for the deviation from the theoretical distribution. Future work should improve our simple covariance model, for example by accounting for the azimuthal dependence of the sensitivity kernel or including prior knowledge based on eddy-resolving ocean circulation models that can capture the non-stationary, non-Gaussian statistics of the real ocean.

3.7 Consistency among receivers and with altimetry

For repeating earthquakes successfully detected at both WAKE and H11, the difference between the two measured T-wave arrival time changes has a standard deviation of 0.06 s (Fig. 2b). This difference exceeds the size of the errors inferred above, so real differences in the travel times to the two receivers likely contribute. The two receivers are roughly 50 km apart in the direction transverse to propagation (Fig. 1b), which is a fair separation for travel time anomalies produced by mesoscale eddies. Differences in the sensitivity kernel for the two receivers might also matter (Fig. 3), with WAKE having a more range-dependent sensitivity and a bigger contribution from higher acoustic modes.

The T-wave travel time change between repeating earthquakes is correlated with the corresponding range-averaged sea level anomaly change from altimetry (Fig. 7). The sea level data is processed as described above, except that we only use the 1st, 11th, and 21st day of each month here. We again remove the seasonal signal from the sea level data because it is dominated by the upper ocean, where the T waves have little sensitivity. We interpolate the sea level data onto each pair's event times and azimuth. The resulting sea level changes and the T-wave travel time anomalies, turned into weighted-average temperature anomalies using the bulk sensitivity, show an approximately multivariate normal distribution with positive covariance. The first singular value of the covariance suggest that a 1 K temperature change in the T-waves data corresponds to 0.75 m sea level change in altimetry. The second singular value is about 15 % of the first, indicating that the T waves supply information that is statistically independent from the sea level data.

We can further interpret the full covariance between these two measurements as a result of the vertical covariance of temperature anomalies in the ocean. If we assume that

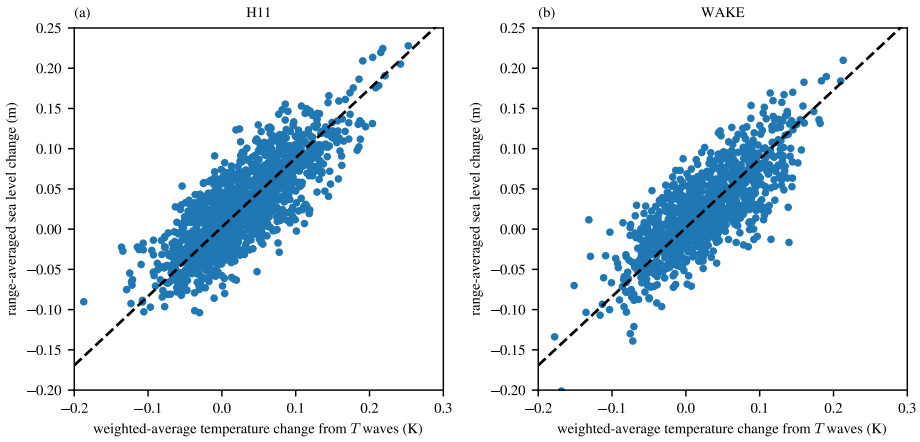

Figure 7: Comparison between the weighted-average temperature change inferred from the T-wave arrival time change between repeating earthquakes and the corresponding range-averaged sea level change from altimetry. This comparison is shown for pairs detected at (a) H11 and (b) WAKE. The black dashed lines show the first principal component direction as an indication of the correlation.

the steric change dominates the sea level change, then the sea level change is essentially a vertically-integrated temperature signal weighted by the thermal expansion coefficient. This contrasts with the T-wave sensitivity kernel that peaks at mid-depth and vanishes at the surface (Fig. 3). But if temperature anomalies are coherent in the vertical, these two distinct weightings will still produce correlated anomalies. Assuming a covariance model in which temperature anomalies decay exponentially with depth and are correlated with some vertical correlation scale, we can predict the resulting covariance of the two measurements. An MLE applied to all pairs that are separated in time by more than a few correlation scales gives a temperature standard deviation of 0.5 K, a decay scale of 520 m, and a vertical correlation scale of 1040 m. These are all plausible numbers, suggesting that the covariance between the two measurements is as expected.

4 Inferred temperature anomalies

The temperature anomalies inferred from the T-wave data are on the order of 0.1 K (Fig. 8a, 9a). Despite being averaged along the T-wave path, these anomalies are dominated by structures that are a few degrees in azimuth and a few tens of days in time, length and time scales consistent with Kuroshio Extension meanders and mesoscale eddies. At times, the inferred temperature differs between a few degrees of azimuth by as

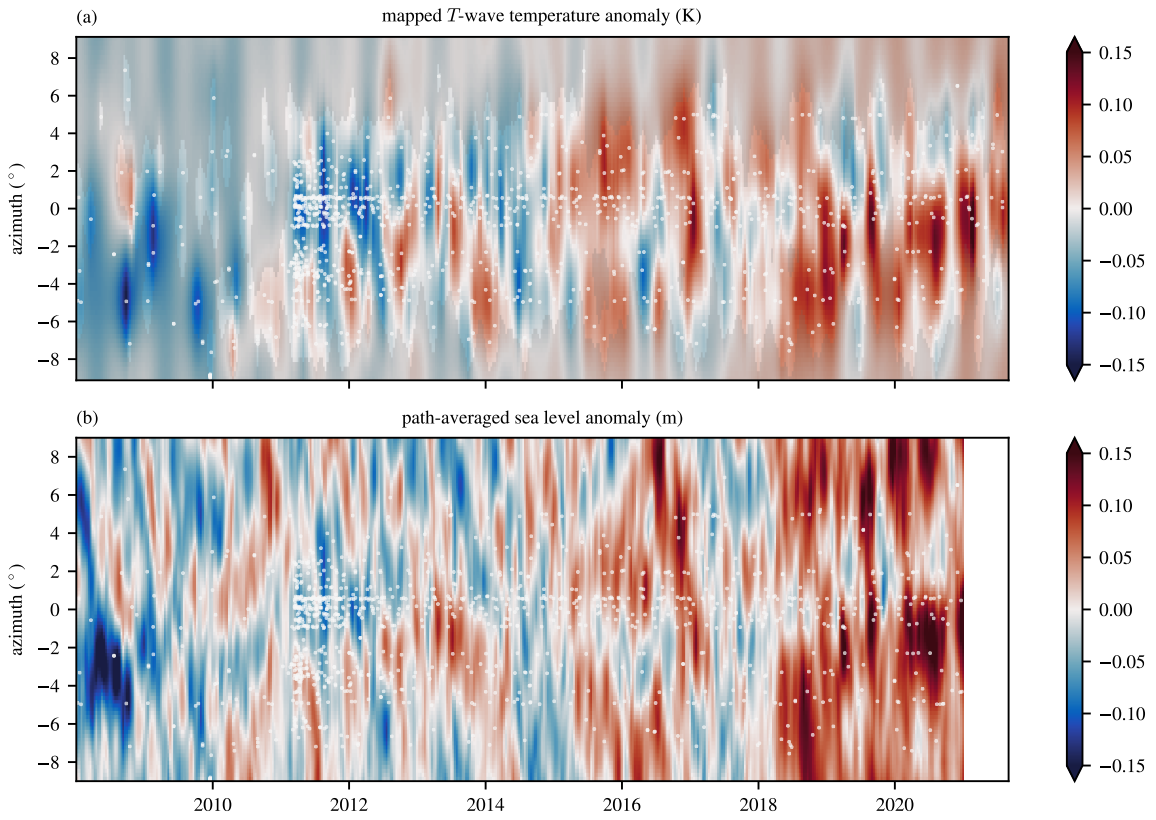

Figure 8: Temperature anomalies inferred from the T waves received at H11 and corresponding sea level anomalies. (a) T-wave temperature anomalies mapped onto a regular time–azimuth grid. The grey shading shows where the posterior variance remains greater than half the prior variance. (b) The range-averaged sea level anomaly, with the seasonal cycle removed yet trend retained. The white dots in both panels show the times and azimuths of earthquakes used in the T-wave inversion. The zero azimuth is set to be the great circle path from the epicenter of the 2011 Tōhoku earthquake. There is no data from the ISC catalog after August 2021.

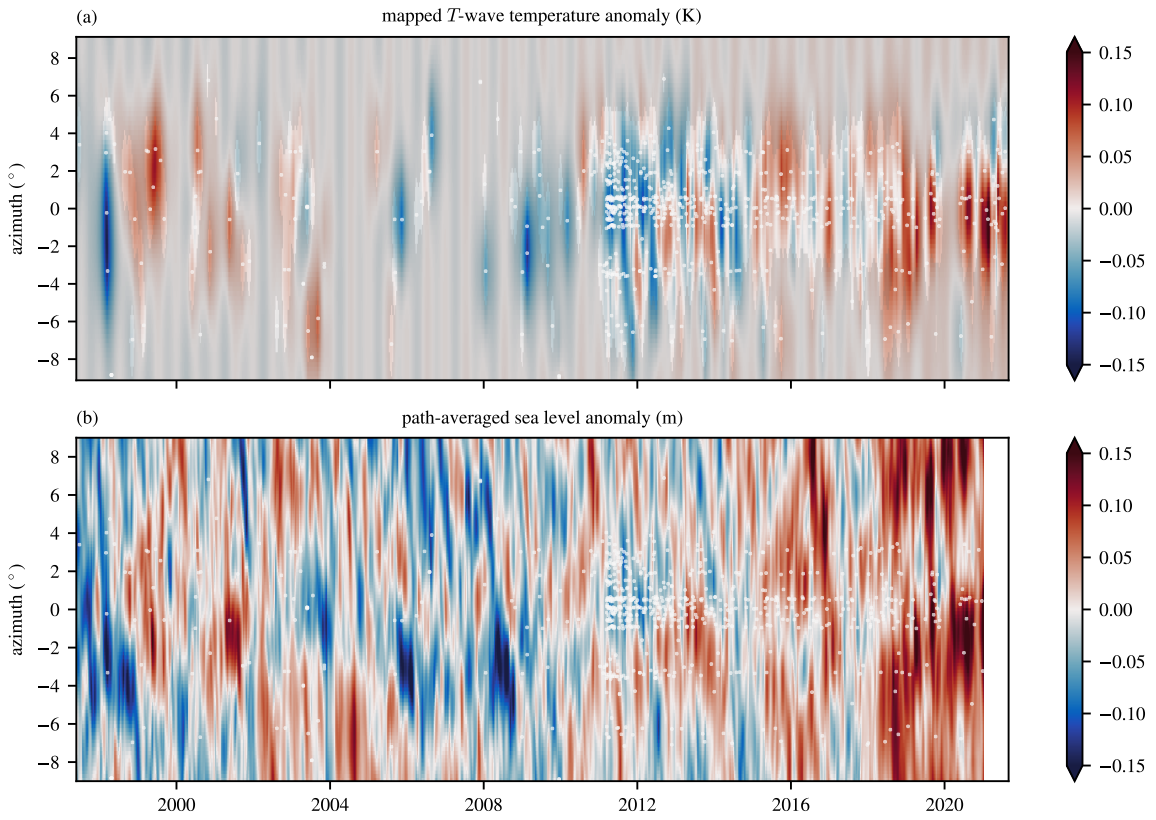

Figure 9: Temperature anomalies inferred from the *T* waves received at WAKE and corresponding sea level anomalies. (a) *T*-wave temperature anomalies mapped onto a regular time–azimuth grid. The grey shading shows where the posterior variance remains greater than half the prior variance. (b) The range-averaged sea level anomaly, with the seasonal cycle removed yet trend retained. The white dots in both panels show the times and azimuths of earthquakes used in the *T*-wave inversion. The zero azimuth is set to be the great circle path from the epicenter of the 2011 Tōhoku earthquake. There is no data from the ISC catalog after August 2021.

much as 0.3 K (e.g., early 2012; cf., Fig. 1b). The degree to which these anomalies are resolved by the *T*-wave data varies in time and azimuth due to the inhomogeneous abundance of repeating earthquakes. The M 9.1 Tōhoku earthquake in March 2011 triggered numerous aftershocks, which markedly increase the resolution in the years following the megathrust event. The anomalies inferred from H11 generally have better resolution, but the WAKE data extends much farther back in time.

Where sufficient resolution is present, the temperature anomalies inferred from the *T*-wave data show a remarkable resemblance to the path-averaged sea level anomalies (Fig. 8b, 9b). While this can be anticipated from the correlation between the measured *T*-wave arrival changes and the range-averaged sea level change, it strengthens our confidence that the inverted *T*-wave temperature anomalies robustly captures a real physical signal. We emphasize that the correlation between the *T*-wave temperature anomalies and path-averaged sea level anomalies is not expected to be perfect—as discussed above, the correlation depends, among other factors, on how strongly deep and column-averaged temperature anomalies are correlated.

The H11 data show predominantly cold anomalies in 2008 to 2012 and predominantly warm anomalies in 2015 to 2021 (Fig. 8a). As a result, over its full duration from 2008 to 2021, the H11 time series exhibits a warming trend of 4.7 ± 1.9 mK yr^{-1}. The WAKE data, however, reveal that this is likely a decadal signal rather than a secular trend. While the coverage from WAKE before 2011 is sparse, there are enough constraints reaching back to 1997 to exclude a trend of the size inferred from H11 to extend over this longer time span. The trend for 1997 to 2021 inferred from the WAKE data is 1.1 ± 1.3 mK yr^{-1}. The decadal-scale variations are likely related to the decadal rearrangements in the Kuroshio Extension path and meander behavior (e.g., Qiu and Chen, 2005; Qiu et al., 2023), but the correspondence between indices commonly used to characterize this variability and the path-averaged signal in the *T*-wave data needs further investigation.

To compare the *T*-wave results to previous estimates and better display the uncertainty, we show time series at a few azimuths (Fig. 10, 11). (Note that our display of the uncertainty in Fig. 10 and 11 differs from that in Wu et al. (2020), Callies et al. (2023), and Wu et al. (2023). In these previous papers, estimates and uncertainties were shown at event times only. Here, we estimate *T*-wave anomalies and their uncertainties on a regular grid. The displayed uncertainty thus captures its increase between event times.) We sample the mapped Argo product by Roemmich and Gilson (2009) and the ECCO state estimate v4r4 (ECCO Consortium et al., 2021; Forget et al., 2015) with the *T*-wave sen-

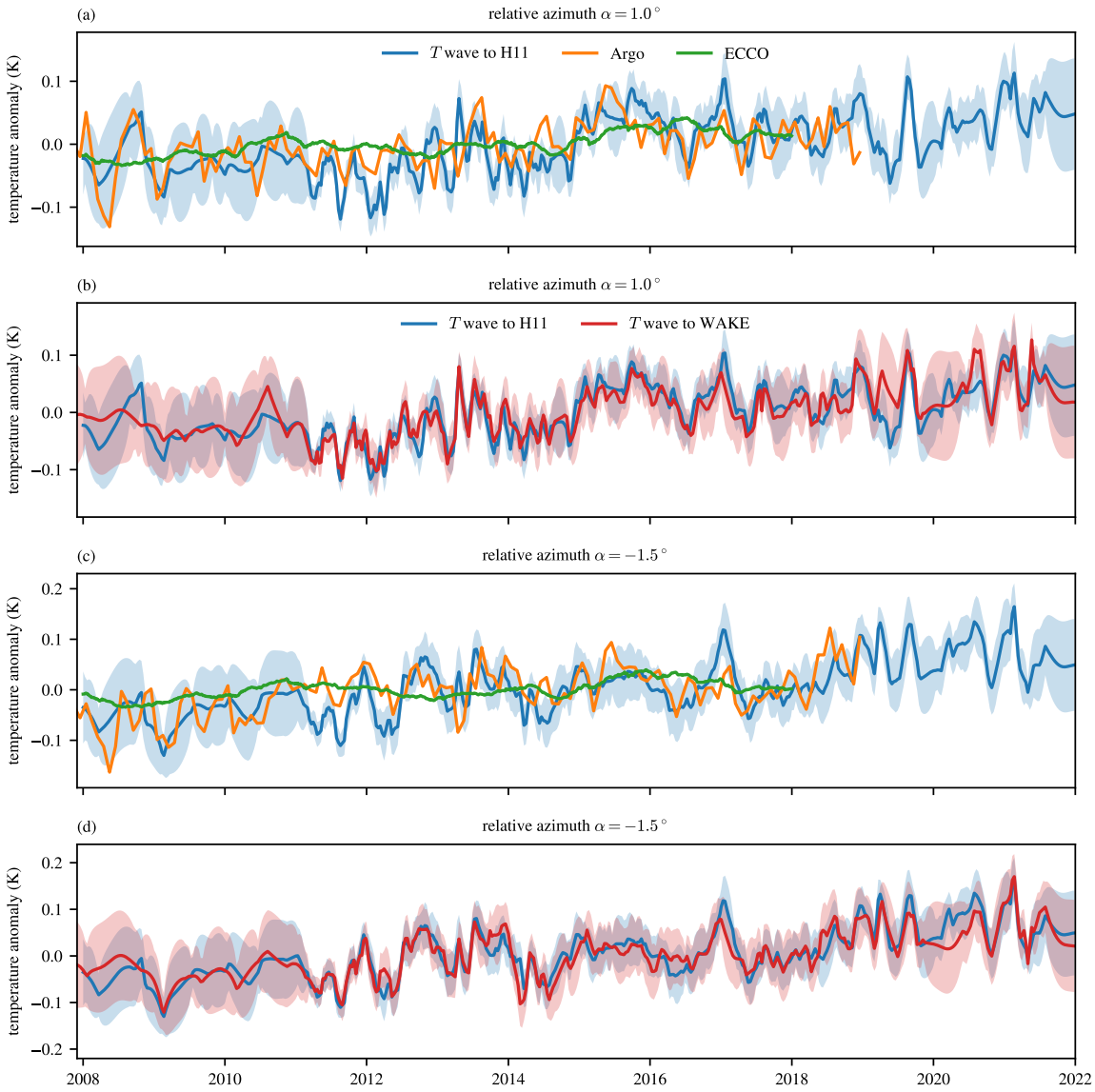

Figure 10: Temperature anomalies at two specific azimuths inferred from T waves and previous estimates. (a,c) Time series at azimuths $\alpha = 1.0$ and -1.5° as inferred from T waves received at H11 and previous estimates sampled with the corresponding T-wave sensitivity kernel. (b,d) Comparison at the same azimuths between the T-wave results inferred from H11 and WAKE. The T-wave estimates are shown on a regular grid, and the shading shows the $\pm 2\sigma$ uncertainty range.

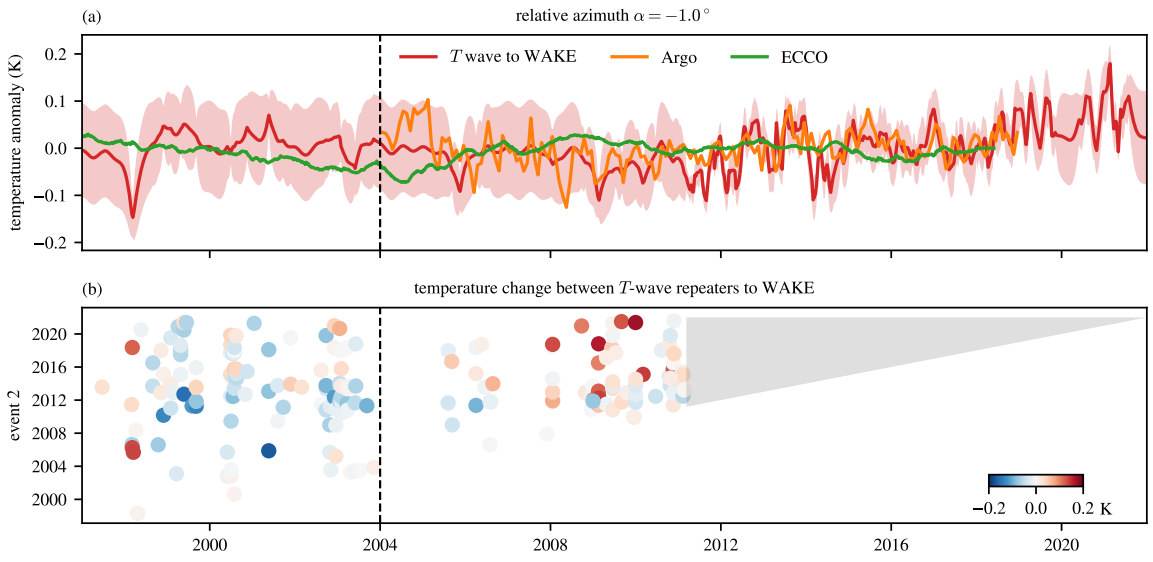

Figure 11: Longer-term constraints from the WAKE station. (a) Temperature anomalies at an azimuth $\alpha = -1.0°$ inferred from T waves received at WAKE and previous estimates sampled with the corresponding T-wave sensitivity kernel. The T-wave estimates are shown on a regular grid, and the shading shows the $\pm 2\sigma$ uncertainty range. (b) Pairs detected at WAKE and the corresponding temperature changes. Only those pairs that involve at least one event prior to the Tōhoku earthquake are shown. The many pairs that are not shown would fall into the gray triangle.

sitivity kernels at a few azimuths to produce equivalent weighted-average temperature anomalies (cf., Wu et al., 2020; Callies et al., 2023; Wu et al., 2023). There is a broad correspondence between the H11 time series and the Argo estimates, both on decadal and inter-annual time scales (Fig. 10a, 11a). Given that Argo floats under-sample the mesoscale meanders and eddies (Fig. 1b), however, the mapped estimate cannot be expected to capture every variation on a sub-seasonal time scale, and the Argo estimate lies well outside of the 95 % confidence range of the T-wave inversion. (Note that no uncertainty estimate is available for the Argo product.) ECCO, fitting a coarse model to available observations, does not capture mesoscale anomalies at all, but there is some correspondence in the inter-annual variations. Over the longer time period, the ECCO and WAKE estimates agree in that they do not display a large secular trend between 1997 and 2021. WAKE samples prior to 2004 are valuable as constraints on the pre-Argo period regardless of its relative sparseness.

As expected from the close correspondence between H11 and WAKE pairs detected

by both (Fig. 2), the time series inferred from the two are consistent with one another (Fig. 10b,d). This is not a trivial result because both stations detect many pairs that the other station does not, and all of these pairs are used in the respective inversion. This confirms that the two stations sample very nearly the same part of the ocean and builds further confidence that the assumptions employed in the inversion are reasonable.

5 Discussion

Travel time changes in *T* waves excited along the Japan Trench and received at Wake Island capture temperature anomalies in the Kuroshio Extension region along the waves' paths. The inferred anomalies vary markedly over just a few degrees of azimuth. At a distance of 3000 km, a degree in azimuth corresponds to a lateral separation of about 50 km between the paths, so these azimuth variations are produced by mesoscale anomalies. This supports the previous attribution by Callies et al. (2023) and Wu et al. (2023) of sharp spikes in the time series of path-averaged temperature anomalies between Sumatra and Cape Leeuwin to mesoscale anomalies. In both regions, the averaging nature of the *T*-wave measurements over travel paths a thousand kilometers long suppresses the mesoscale anomalies relative to their local values by a factor of ten or so, yet the mesoscale anomalies remain a leading-order signal. This is in contrast to the ATOC results from the Northeast Pacific, where mesoscale eddies are relatively weak and travel time anomalies varied much more smoothly (The ATOC Consortium, 1998; Dushaw et al., 1999). These results further emphasize the importance of widespread sampling to avoid the aliasing of mesoscale anomalies when attempting to constrain a large-scale signal, especially in eddy-rich regions in the vicinity of western boundary currents and the Southern Ocean.

While we obtain constraints from a total of 1566 *T*-wave pairs at H11 and 1201 *T*-wave pairs at WAKE, these numbers are less than a tenth of the number of coherent pairs detected at the land stations. This shortfall is likely due to a combination of the following explanations:

1. Many of the *P*-wave pairs may be false detections. Because we also require coherent waveforms at the *T*-wave receiver to consider a pair measurement reliable, we use somewhat less stringent criteria for the detection of repeaters at land stations than previous studies looking to identify repeaters from land stations only (e.g., Uchida and Bürgmann, 2019; Igarashi, 2020).

2. Large-amplitude *T* waves are excited only by earthquakes that occur sufficiently far east of the trench, which allows efficient coupling of the seismic waves to near-axis waves in the ocean's sound channel (e.g., Okal, 2008). Events that occur too far east and too deep are not ideal either because the seismic waves then suffer substantial loss along their longer solid-earth path. Repeaters not optimally located in relation to the trench produce weak *T* waves that give rise to noisy signals at the receivers.

3. While the source properties are sufficiently similar between pairs to produce coherent *P*-wave pairs, they may be sufficiently different for many pairs to produce *T* waves with substantially different waveforms. *T* waves are understood to be excited along a section of a trench that exhibits complicated topographic variations, a process that might make the waveforms of *T* waves an even more sensitive function of the source properties than those of *P* waves.

4. For many pairs, the change in the ocean's sound speed field may cause changes in the received waveforms even if the excited *T* waves are highly coherent between the events. There are distinct processes that might cause this loss of coherence:

   (a) The fundamental acoustic mode that tends to dominate the *T*-wave signal at low frequencies experiences a greater shift in its travel time at high frequencies than at low frequencies when temperature anomalies are surface-intensified. This property of *T* waves appears to be the primary cause for cycle skipping and is the basis of our correction scheme (Callies et al., 2023). It also reduces the coherence of the waveforms.

   (b) If higher acoustic modes contribute to the received waveform, they would experience different travel time shifts than the fundamental mode, so the superimposed arrival pattern will be less coherent than it would be if it consists of the fundamental mode only. Callies et al. (2023) and Wu et al. (2023) attributed the loss of coherence at frequencies higher than 4 Hz to this effect. Higher modes interact strongly with the bottom at low frequencies but progressively contract into the sound channel as the frequency is increased. They can also be excited by mode coupling when *T* waves encounter bathymetry changes.

   (c) The excitation of *T* waves along a section of the trench means that the received waveforms have contributions from a range of azimuths (de Groot-Hedlin and Orcutt, 1999). This raises the possibility that different parts of this multipath

experience different temperature changes between the repeating events. If the excitation region is a few tens of kilometers wide, mesoscale anomalies will contribute substantially to such variations across the multipath. If the excitation is substantially narrower, sharp fronts and internal waves can still produce such variations and suppress the waveform coherence.

(d) Mesoscale anomalies and shifts in the Kuroshio Extension cause lateral deflections of the *T*-wave paths (e.g., Munk, 1980; Dushaw, 2014; Heaney and Campbell, 2016) that change between the repeating events. Sufficiently large deflections could produce lensing and thus changes in the received waveforms.

The location of earthquakes in relation to the trench clearly matters: earthquakes that produce a successful *T*-wave measurement are preferentially located in a band some 200 km east of the trench (Fig. 1a). This cannot be the only reason, however, for the reduction of *T*-wave coherence. We find many families of *P*-wave repeaters with more than two members. Among the pairs that produce a coherent *T*-wave signal, there are many families of connected pairs. These families consist of events that are connected by pairs that pass our CC thresholds for at least one *P*-wave station and the *T*-wave receiver. These families of events therefore likely share very similar source properties, so the excitation of *T* waves should be similarly efficient. Yet, for H11, out of 5214 possible pairs that can be formed by these families of events and that have an SNR greater than two at the receiver, only 1566 events pass our *T*-wave CC threshold of 0.6. We therefore surmise that the waveform coherence is reduced substantially by the propagation through a changing ocean.

The proposition that the *T*-wave propagation through a changing ocean reduces the coherence between repeating pairs is further supported by the observation that the coherence between repeaters systematically drops with the amount of time between the repeating events (Fig. 12). We again consider the 5214 possible repeating pairs between events that are involved in at least one successful detection at H11. Of the potential pairs with a repeat interval less than 10 days, 92 % have a CC greater than 0.6. For those with a repeat interval of 20 to 30 days, the CC passes this threshold at a rate of 77 % and 57 %, respectively. For pairs with a longer repeat interval, making up the bulk of the total population, this rate drops to 28 %. This drop in waveform coherence over a time scale comparable to the evolution time scale of Kuroshio Extension meanders and mesoscale eddies suggests that these changes in the ocean's sound speed field affect the waveform

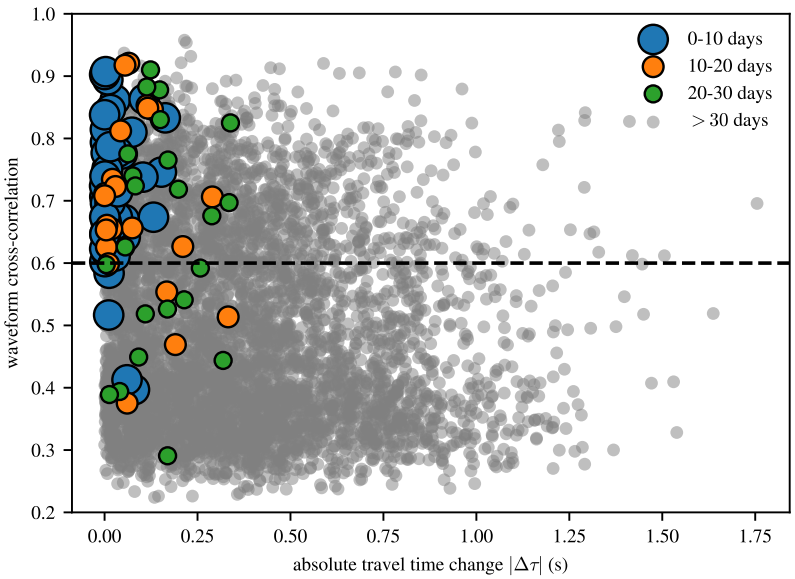

Figure 12: Drop in *T*-wave coherence with the repeat interval. Shown is the peak CC for a population of 5214 potential pairs between events that are part of at least one successful detection at H11. We estimate the *T*-wave travel time change of these pairs using the inverted results based on the successful measurements. The potential pairs are split into those with a repeat interval of <10 days (blue), 10 to 20 days (orange), 20 to 30 days (green), and > 30 days (transparent gray). The horizontal dashed line highlights the CC threshold for *T*-wave detection.

coherence. This effect should be investigated further in future work because it raises the possibility that there is a selection bias for pairs between times at which the current and eddies had similar configurations. Furthermore, understanding this effect better may allow extracting usable information from these many potential pairs. It should also be kept in mind, however, that the mesoscale variability in the Kuroshio Extension region is exceptionally strong, so the loss of coherence seen here is likely rather extreme compared to the rest of the global ocean.

T-wave coherence also varies with azimuth, likely due to local bathymetry, and it is not always better at H11 than at WAKE (Fig. 13). At both receivers, most detections are recorded around zero azimuth, the azimuth of the M 9.1 Tōhoku earthquake in 2011 that caused a large number of aftershocks. Splitting the azimuth range into 0.6° bins, we find that H11 detects most pairs between 0.3° and 0.9°—more than double the number of detections at WAKE and quadruple the number of common detections in the same bin. WAKE detections, in contrast, maximize between −0.3° and 0.3° at a number also nearly

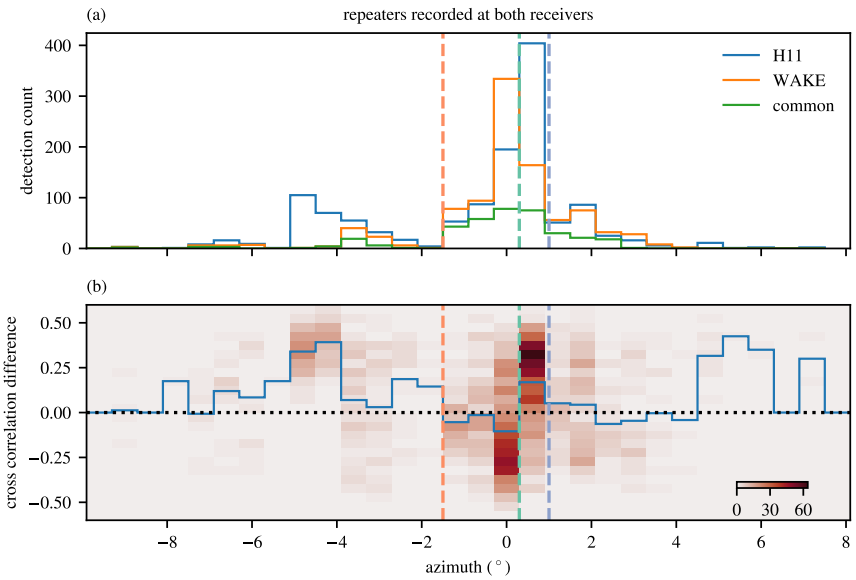

Figure 13: Change in *T*-wave coherence with azimuth. (a) Histograms of the number of repeaters detected at H11, WAKE, and both for a total of 1261 pairs recorded by both receivers. (b) Waveform cross-correlation differences between H11 and WAKE for 1830 pairs detected by at least one receiver but available at both. The vertical dashed lines highlight azimuths of 1.0° (blue), 0.3° (green), and −1.5° (orange). The azimuth calculation is referenced to H11. The bin size in azimuth is 0.6°, and the blue curve in (b) shows the mean difference for each bin.

double that of H11 and quadruple that of common detections. Here, we only consider pairs for which the *T* waves were received at both stations, excluding periods when one of the stations was not available. Clearly, *T* waves display a different amount of coherence at the two stations, despite the small azimuth difference. This shift is seen clearly in a histogram of the differences in the CC for all pairs detected by at least one receiver (Fig. 13b). We speculate that differences in the bathymetry near the receivers explains this shift in *T*-wave coherence. The sensitivity kernels for the two receivers at $\alpha = 1.0°$ do show a larger amount of interaction with bathymetry for WAKE than for H11 (Fig. 3a,b). Further work is needed, however, to fully understand these effects.

6 Conclusions

Seismically generated sound waves propagating from the Japan Trench to Wake Island can help constrain the deep temperature variability in the Kuroshio Extension region. The

change in the travel time of these *T* waves between repeating earthquakes gives a measurement of a weighted-average temperature change along the waves' path. Thousands of such measurements can be made and combined in a carefully calibrated inversion to estimate the time and azimuth dependence of these path-averaged temperature anomalies. Smaller earthquakes can be detected at the CTBTO station H11, but the island station WAKE has a longer record and allows constraints back to the pre-Argo period. Analog records may yield valuable constraints going even further back in time.

A comparison with altimetry reveals similarities with the *T*-wave measurements, suggesting that meanders of the Kuroshio Extension and mesoscale eddies produce a large part of the signal. This variability must be captured if long-term changes in the deep ocean are to be confidently inferred. The array of Argo floats, however, captures only part of this variability. Even in its current configuration with some 4000 floats globally, mesoscale eddies are not resolved. As a result, mapped Argo products capture some but not all of the variability seen in the *T*-wave measurements. Core Argo floats also only sample to 2000 m depth. The *T*-wave measurements thus offer valuable constraints that should be combined with hydrographic measurements, for example in the ECCO framework (Forget et al., 2015).

This successful application of seismic ocean thermometry in the Kuroshio Extension region encourages a geographic expansion of the approach. While the seismicity produced by the 2011 Tōhoku earthquake and the extensive seismic station network on Japan are advantageous for seismic ocean thermometry, the vigorous variability produced by the Kuroshio Extension appears to substantially reduce the number of measurements by substantially deforming the waveforms between repeating earthquakes. Applying this method in regions with more modest seismicity but also less vigorous mesoscale eddies may therefore be expected to still produce a large number of useful constraints on changes in deep ocean temperatures.

Acknowledgments

This material is based upon work supported in part by the Resnick Sustainability Institute and in part by the National Science Foundation under Grant No. OCE-2023161. The computations presented here were conducted in the Resnick High Performance Center, a facility supported by Resnick Sustainability Institute at the California Institute of Technology.

Data availability statement

The IMS hydrophone data are available directly from the CTBTO upon request and signing a confidentiality agreement to access the virtual Data Exploitation Centre (vDEC: https://www.ctbto.org/resources/for-researchers-experts/vdec). All seismic data were downloaded through IRIS Data Management Center https://ds.iris.edu/ds/nodes/dmc/, including the seismic networks II (GSN; https://doi.org/10.7914/SN/II), IU, PS, G (https://doi.org/10.14470/TR560404). Global Seismographic Network (GSN) is a cooperative scientific facility operated jointly by the Incorporated Research Institutions for Seismology (IRIS), the United States Geological Survey (USGS) and the National Science Foundation (NSF), under Cooperative Agreement EAR-1261681. Bathymetry data were downloaded from and freely available at https://download.gebco.net/. The Argo data were downloaded from https://sio-argo.ucsd.edu/RG_Climatology.html. Argo data were collected and made freely available by the International Argo Program and the national programs that contribute to it (http://www.argo.ucsd.edu, http://argo.jcommops.org). The Argo Program is part of the Global Ocean Observing System. The ECCO data were available at https://podaac.jpl.nasa.gov/dataset/ECCO_L4_TEMP_SALINITY_05DEG_DAILY_V4R4. The processing code is available at https://github.com/joernc/sot.

References

Callies, J., W. Wu, S. Peng, Z. Zhan (2023) Vertical-Slice Ocean Tomography with Seismic Waves. *Geophysical Research Letters* 50 (8), e2023GL102881.

De Groot-Hedlin, C. D., J. A. Orcutt (1999) Synthesis of Earthquake-Generated T-waves. *Geophysical Research Letters* 26 (9), 1227–1230.

Dushaw, B. et al. (1999) Multimegameter-Range Acoustic Data Obtained by Bottom-Mounted Hydrophone Arrays for Measurement of Ocean Temperature. *IEEE Journal of Oceanic Engineering* 24 (2), 202–214.

Dushaw, B. D. (2014) Assessing the Horizontal Refraction of Ocean Acoustic Tomography Signals Using High-Resolution Ocean State Estimates. *The Journal of the Acoustical Society of America* 136 (1), 122–129.

ECCO Consortium, I. Fukumori, O. Wang, I. Fenty, G. Forget, P. Heimbach, R. M. Ponte (2021) *Synopsis of the ECCO Central Production Global Ocean and Sea-Ice State Estimate, Version 4 Release 4*. Zenodo.

Forget, G., J.-M. Campin, P. Heimbach, C. N. Hill, R. M. Ponte, C. Wunsch (2015) ECCO Version 4: An Integrated Framework for Non-Linear Inverse Modeling and Global Ocean State Estimation. *Geoscientific Model Development* 8 (10), 3071–3104.

Gill, A. E., P. P. Niiler (1973) The Theory of the Seasonal Variability in the Ocean. *Deep Sea Research and Oceanographic Abstracts* 20 (2), 141–177.

Hansen, J., G. Russell, A. Lacis, I. Fung, D. Rind, P. Stone (1985) Climate Response Times: Dependence on Climate Sensitivity and Ocean Mixing. *Science* 229 (4716), 857–859.

Heaney, K. D., R. L. Campbell (2016) Three-Dimensional Parabolic Equation Modeling of Mesoscale Eddy Deflection. *The Journal of the Acoustical Society of America* 139 (2), 918–926.

Held, I. M., M. Winton, K. Takahashi, T. Delworth, F. Zeng, G. K. Vallis (2010) Probing the Fast and Slow Components of Global Warming by Returning Abruptly to Preindustrial Forcing. *Journal of Climate* 23 (9), 2418–2427.

Igarashi, T. (2020) Catalog of Small Repeating Earthquakes for the Japanese Islands. *Earth, Planets and Space* 72 (1), 73.

Kaipio, J. P., E. Somersalo (2005) *Statistical and Computational Inverse Problems*. Springer.

Kuusela, M., M. L. Stein (2018) Locally Stationary Spatio-Temporal Interpolation of Argo Profiling Float Data. *Proceedings of the Royal Society A: Mathematical, Physical and Engineering Sciences* 474 (2220), 20180400.

Meyssignac, B. et al. (2019) Measuring Global Ocean Heat Content to Estimate the Earth Energy Imbalance. *Frontiers in Marine Science* 6, 432.

Mizuno, K., W. B. White (1983) Annual and Interannual Variability in the Kuroshio Current System. *Journal of Physical Oceanography* 13 (10), 1847–1867.

Munk, W., C. Wunsch (1979) Ocean Acoustic Tomography: A Scheme for Large Scale Monitoring. *Deep Sea Research Part A. Oceanographic Research Papers* 26 (2), 123–161.

Munk, W. H. (1980) Horizontal Deflection of Acoustic Paths by Mesoscale Eddies. *Journal of Physical Oceanography* 10 (4), 596–604.

Nichols, S. M., D. L. Bradley (2017) In Situ Shape Estimation of Triangular Moored Hydrophone Arrays Using Ambient Signals. *IEEE Journal of Oceanic Engineering* 42 (4), 923–935.

Nocedal, J., S. J. Write (2006) *Numerical Optimization*. Springer New York.

Nonaka, M., H. Nakamura, Y. Tanimoto, T. Kagimoto, H. Sasaki (2006) Decadal Variability in the Kuroshio–Oyashio Extension Simulated in an Eddy-Resolving OGCM. *Journal of Climate* 19 (10), 1970–1989.

Okal, E. A. (2008) The Generation of *T* Waves by Earthquakes. In: *Advances in Geophysics*. Ed. by R. Dmowska. Vol. 49. Elsevier, p. 1–65.

Palmer, M. D., D. J. McNeall, N. J. Dunstone (2011) Importance of the Deep Ocean for Estimating Decadal Changes in Earth's Radiation Balance. *Geophysical Research Letters* 38 (13).

Qiu, B., S. Chen (2005) Variability of the Kuroshio Extension Jet, Recirculation Gyre, and Mesoscale Eddies on Decadal Time Scales. *Journal of Physical Oceanography* 35 (11), 2090–2103.

Qiu, B., S. Chen, E. Oka (2023) Why Did the 2017 Kuroshio Large Meander Event Become the Longest in the Past 70 Years? *Geophysical Research Letters* 50 (10), e2023GL103548.

Riser, S. C. et al. (2016) Fifteen Years of Ocean Observations with the Global Argo Array. *Nature Climate Change* 6 (2), 145–153.

Roemmich, D., J. Gilson (2009) The 2004–2008 Mean and Annual Cycle of Temperature, Salinity, and Steric Height in the Global Ocean from the Argo Program. *Progress in Oceanography* 82 (2), 81–100.

Rossby, T., C. N. Flagg, K. Dohan, S. Fontana, R. Curry, M. Andres, J. Forsyth (2019) Oleander Is More than a Flower: Twenty-Five Years of Oceanography Aboard a Merchant Vessel. *Oceanography* 32 (3), 126–137.

Saba, V. S. et al. (2016) Enhanced Warming of the Northwest Atlantic Ocean under Climate Change. *Journal of Geophysical Research: Oceans* 121 (1), 118–132.

Sanz-Alonso, D., A. M. Stuart, A. Taeb (2023) *Inverse Problems and Data Assimilation*. URL: `http://arxiv.org/abs/1810.06191` (visited on 03/20/2023). Preprint.

Sugimoto, S., K. Hanawa, T. Watanabe, T. Suga, S.-P. Xie (2017) Enhanced Warming of the Subtropical Mode Water in the North Pacific and North Atlantic. *Nature Climate Change* 7 (9), 656–658.

Talley, L. et al. (2016) Changes in Ocean Heat, Carbon Content, and Ventilation: A Review of the First Decade of GO-SHIP Global Repeat Hydrography. *Annual Review of Marine Science* 8 (1), 185–215.

The ATOC Consortium (1998) Ocean Climate Change: Comparison of Acoustic Tomography, Satellite Altimetry, and Modeling. *Science* 281 (5381), 1327–1332.

Trenberth, K. E., J. T. Fasullo, M. A. Balmaseda (2014) Earth's Energy Imbalance. *Journal of Climate* 27 (9), 3129–3144.

Uchida, N., R. Bürgmann (2019) Repeating Earthquakes. *Annual Review of Earth and Planetary Sciences* 47 (1), 305–332.

Von Schuckmann, K. et al. (2016) An Imperative to Monitor Earth's Energy Imbalance. *Nature Climate Change* 6 (2), 138–144.

Wu, L. et al. (2012) Enhanced Warming over the Global Subtropical Western Boundary Currents. *Nature Climate Change* 2 (3), 161–166.

Wu, W., Z. Shen, S. Peng, Z. Zhan, J. Callies (2023) Seismic Ocean Thermometry Using CTBTO Hydrophones. *Submitted*.

Wu, W., Z. Zhan, S. Peng, S. Ni, J. Callies (2020) Seismic Ocean Thermometry. *Science* 369 (6510), 1510–1515.

Wunsch, C. (2006) *Discrete Inverse and State Estimation Problems: With Geophysical Fluid Applications*. Cambridge University Press.

Wunsch, C., D. Stammer (1998) Satellite Altimetry, the Marine Geoid, and the Oceanic General Circulation. *Annual Review of Earth and Planetary Sciences* 26 (1), 219–253.

Yasuda, I., K. Okuda, M. Hirai (1992) Evolution of a Kuroshio Warm-Core Ring—Variability of the Hydrographic Structure. *Deep Sea Research Part A. Oceanographic Research Papers* 39 (Suppl. 1), S131–S161.